PAPER

Check for updates

One-step hydrothermal synthesis of a Ni_3S_2–$FeMoO_4$ nanowire–nanosheet heterostructure array for synergistically boosted oxygen evolution reaction†

Han Chen,‡[ab] Jing Zhang,‡[bc] Rui Wan,[bc] Xiang Zhang,[bc] Qijun Pan,[bc] Mingtao Li*[d] and Bin Chen [iD] *[bc]

A key factor for boosting oxygen evolution reaction (OER) is the design of heterostructures with steerable defects and interfaces, which can optimize the surface electronic structures and achieve efficient water splitting to produce hydrogen fuel. Herein, we propose a novel one-step hydrothermal approach to fabricate hierarchical Ni_3S_2 nanowires with an S-doped $FeMoO_4$ nanosheet heterostructure array *in situ* on Ni–Fe foam (NFF) as a self-standing electrode for synergistically boosted OER. The metalloid Ni_3S_2 nanowires with good conductivity support the $FeMoO_4$ nanosheets and act as high-speed paths for the charge transfer. Numerous ultrathin S-doped $FeMoO_4$ nanosheets are uniformly distributed on each Ni_3S_2 nanowire to form heterostructures with larger specific surface area and more revealable active sites, and a strong synergistic effect is created at the heterostructure interfaces to further promote the OER dynamics. Additionally, the NFF serves as the conductive support substrate and simultaneously provides the Ni and Fe sources for the self-growing Ni_3S_2–$FeMoO_4$, leading to a structurally-integrated electrode with low contact resistance, fast mass transfer, and good stability. Therefore, the Ni_3S_2–$FeMoO_4$/NFF electrode offers a low overpotential of 331 mV to achieve 500 mA cm^{-2} and long-term stability at 100 mA cm^{-2} level for more than 40 h. This work provides insight into the heterostructure of molybdate and sulfide, and a deep understanding of the significance of the synergism in OER operation.

Regarding the escalating energy crises, there is an urgent need to explore and develop clean and efficient energy conversion technologies.[1] Electrochemical water splitting driven by renewable electricity has been widely regarded as an effective strategy to produce carbon-free hydrogen. The overall efficiency of water electrolysis is greatly hindered by the oxygen evolution reaction (OER) owing to its sluggish four-proton-couple electron transfer progress.[2] Electrocatalysts can significantly decrease the energy barrier and accelerate OER operation. The benchmark electrocatalysts rely heavily on iridium and ruthenium-based oxides. However, their large-scale application is unfortunately limited due to their resource scarcity and expensive cost.[3] Therefore, this issue inspires interest in exploring abundant non-precious metal electrocatalysts.

Currently, transition metal-based materials, including layered double hydroxides,[4] oxides,[5–7] phosphides,[8] and sulfides,[9–11] have been widely studied as alternative electrocatalysts. Among them, Ni_3S_2 has attracted increasing attention due to its high electrical conductivity and unique metallic feature.[12] However, the relatively low intrinsic activity and poor stability of Ni_3S_2 limit the industrial application for water electrolysis. Numerous efforts have been devoted to heterostructure engineering by combining Ni_3S_2 with other active materials to further promote the OER activity.[13] Recently, Mo-based oxides have been combined with Ni_3S_2 to obtain heterostructures, which could form strong synergistic effect to promote the OER activity and the electrochemical durability.[14] For example, hierarchical MoO_x/MoS_2 decorated NiO_x/Ni_3S_2 nanorods have been prepared by a hydrothermal reaction and surface reconfiguration strategy, which exhibits a remarkable OER performance and excellent stability.[15] Nevertheless, these Ni_3S_2-based heterostructures were mostly fabricated by complex multi-steps of preparing Ni_3S_2 support matrix and then

[a]Institutes of Physical Science and Information Technology, School of Materials Science and Engineering, Anhui University, Hefei 230601, P. R. China

[b]Key Laboratory of Materials Physics, Anhui Key Laboratory of Nanomaterials and Nanotechnology, Institute of Solid State Physics, HFIPS, Chinese Academy of Sciences, 350 Shushanhu Road, Hefei, Anhui 230031, P. R. China. E-mail: bchen@issp.ac.cn

[c]University of Science and Technology of China, 96 Jinzhai Road, Hefei, Anhui 230026, P. R. China

[d]School of Mechanical and Resource Engineering, Wuzhou University, Wuzhou 543002, China. E-mail: mtli@gxuwz.edu.cn

† Electronic supplementary information (ESI) available. See DOI: https://doi.org/10.1039/d4ra01770f

‡ These authors contributed equally to this work.

synthesizing the active materials on Ni_3S_2. Unfortunately, little attention has been paid to the remarkable achievement of obtaining heterostructures of nanowires/nanosheets through a one-step method. On the other hand, it is difficult to accurately control the heterostructure engineering due to the unsuitable lattice matching, resulting in limited interface and weak synergistic effect. Thus, the electrocatalytic activity of these Ni_3S_2-based heterostructures are still insufficient for industrial application that needs to be operated at a high current density more than 500 mA cm^{-2}. Therefore, it is urgently desired to explore a rational and straightforward synthesis strategy to construct novel Ni_3S_2-based heterostructures for realizing industrial application of water electrolysis.

Herein, we design and fabricate a novel hierarchical heterostructure of Ni_3S_2 nanowires coated with S-doped $FeMoO_4$ nanosheets *in situ* on nickel-iron foam (denoted as Ni_3S_2–$FeMoO_4$/NFF) by an effective one-step hydrothermal strategy, which obviously reduced the difficulty of preparation and saved time out (Fig. 1). The Ni–Fe foam (NFF) not only serves as the conductive support substrate, but also simultaneously provides the Ni and Fe sources for the self-growing Ni_3S_2–$FeMoO_4$ heterostructures, leading to a structurally-integrated electrode with low contact resistance and good mechanical stability. Importantly, the S-doped $FeMoO_4$ ultrathin nanosheets have been successfully integrated with Ni_3S_2 nanowires to form heterostructures. In addition, the 3D hierarchical, self-supported, and binder-free nanowire–nanosheet architectural morphology endows the obtained electrode with abundant active sites, rapid bubbles release, and timely electrolyte diffusion. As a result, the Ni_3S_2–$FeMoO_4$ heterostructures array electrode demonstrates a superb OER performance with ultralow potential and good long-time stability.

The typical Ni_3S_2–$FeMoO_4$ nanowire–nanosheet array electrode was *in situ* synthesized on the NFF by a facile one-step hydrothermal method for 10 h. Scanning electron microscopy (SEM) shows that the pristine NFF consists of numerous interconnected skeletons with porous surface (Fig. S1†). XRD pattern reveals that three prominent characteristic peaks are assignable to the metallic NFF (PDF#38-0419), while the weak diffraction peaks adopted to Ni_3S_2 (PDF#85-1802) and $FeMoO_4$ (PDF#22-0629) can be observed, indicating the Ni_3S_2–$FeMoO_4$ is successfully grown on NFF (Fig. S2†). To eliminate the influence of NFF, XRD patterns of the catalysts powder peeled from NFF were employed to characterize the crystalline phases. As depicted in Fig. 2a, the distinct and sharp peaks can be assigned to the corresponding crystal planes of Ni_3S_2 and the other peaks
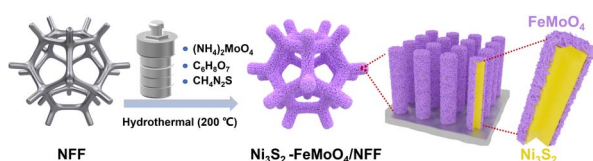

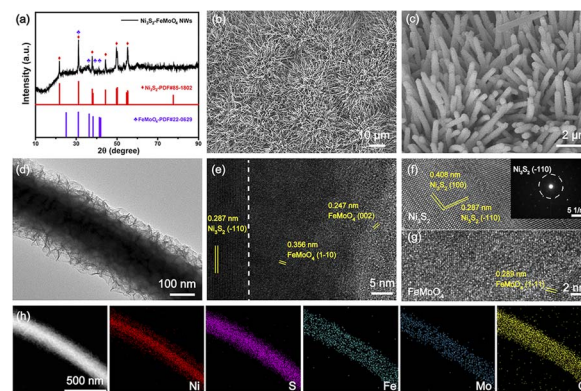**Fig. 2** Structural characterizations of Ni_3S_2–$FeMoO_4$. (a) XRD patterns. (b) and (c) SEM images with different magnifications. (d) TEM image. (e) HRTEM image. (f) HRTEM image of Ni_3S_2 region of the Ni_3S_2–$FeMoO_4$, the inset image is selected area diffraction pattern of Ni_3S_2. (g) HRTEM image of $FeMoO_4$ region of the Ni_3S_2–$FeMoO_4$. (h) HAADF-STEM image and the corresponding mapping elements of Ni, S, Fe, Mo and O.

are assigned to $FeMoO_4$. SEM images unveil that the Ni_3S_2–$FeMoO_4$ has a 3D coral-like nanowire architecture with average length and diameter of 15 μm and 300 nm, respectively (Fig. 2b and c). Transmission electron microscopy (TEM) in Fig. 2d illustrates numerous ultrathin nanosheets are uniformly distributed on each nanowire to form core–shell heterostructures. The high-resolution TEM (HRTEM) image obviously shows the heterointerface, where the left crystalline region is the nanowire and the right low-crystallinity region is the nanosheet (Fig. 2e). Notably, the obtained lattice fringes in left region exhibit the lattice distance of 0.287 nm, well aligned with the (−1 1 0) plane of Ni_3S_2, whereas the interplanar spacing of 0.247 nm and 0.356 nm correspond to the (0 0 2) and (1 −1 0) planes of $FeMoO_4$ in right region. The enlarged HRTEM images further confirm that the hierarchical Ni_3S_2–$FeMoO_4$ core–shell heterostructures have been successfully prepared (Fig. 2f and g). Additionally, the selected area electron diffraction (SAED) agrees well with Ni_3S_2, indicating the low crystallinity of $FeMoO_4$ nanosheets. High-angle annular dark field scanning transmission electron microscopy (HAADF-STEM) image reveals the Ni_3S_2–$FeMoO_4$ more clearly (Fig. 2h). The corresponding elemental mapping images show the Ni and S elements predominantly localize in the core nanowire region, while Mo, O, and Fe elements are mainly distributed along the outer nanosheets region with slight S element, which further elucidates the compositional distribution of Ni_3S_2 nanowire and S-doped $FeMoO_4$ nanosheet core–shell structure.

X-ray photoelectron spectroscopy (XPS) explored the elemental valence and electronic interactions on the Ni_3S_2–$FeMoO_4$/NFF. The XPS full spectrum further demonstrates that Ni, Fe, Mo, O, and S are present in Ni_3S_2–$FeMoO_4$ (Fig. S3a†). The Ni 2p spectrum is fitted in Fig. S3b,† the characteristic peaks at 855.5 eV ($2p_{3/2}$) and 873.08 eV ($2p_{1/2}$) are assigned to Ni^{2+}, respectively, while the peaks at 856.61 eV ($2p_{3/2}$) and 874.53 eV ($2p_{1/2}$) are assigned to Ni^{3+}. The S 2p XPS spectrum is shown in Fig. S3c,† and the peaks observed at 169.18 eV and

Fig. 1 Schematic illustration for the synthesis of Ni_3S_2–$FeMoO_4$/NFF electrode.

168.02 eV are attributed to the S $2p_{1/2}$ and $2p_{3/2}$ bimodal peaks, respectively, which are indicative of the sulfite (SO_3^{2-}) species due to surface oxidation in air. Similarly, the peaks at 163.03 eV and 161.78 eV are assigned to the disulfide (S_2^{2-}) species. It is shown that the reaction of S element with Ni produces S metallized metal.[16] In Fig. S3d and e,† the Fe 2p and Mo 3d spectra further confirm the nanosheets are $FeMoO_4$. In addition, O 1s XPS spectrum in Fig. S3f† consists of three characteristic peaks of metal–oxygen bond (530.14 eV), hydroxides bond (530.77 eV) and oxygen vacancy (531.55 eV), indicating the incorporation of S in the $FeMoO_4$.[17] All these results demonstrate the Ni_3S_2–$FeMoO_4$ nanowire–nanosheet array successfully grow on the NFF by one-step hydrothermal method.

To explore the evolutionary process detail of morphology, the XRD patterns and SEM images of Ni_3S_2–$FeMoO_4$ with different hydrothermal treatment times were displayed in Fig. S4 and S5,† respectively. The XRD results demonstrate that the electrocatalyst crystallized after 10 h. The morphology started from smooth and bulky nanowires structure for 4 h (Fig. S5a and b†). As the preparation time increased to 10 h, the coral-like structures of nanowires coated with numerous nanosheets could be observed on the NFF (Fig. S5c and d†). When the hydrothermal time further reach to 16 h, the nanowire–nanosheet structures continued to grow and became longer with a smaller diameter, ultimately resulting in collapsed network (Fig. S5e and f†). In addition, a contrast sample was prepared by the same condition except for using Ni foam (NF), which was denoted as NiMo-OS/NF.[18] The SEM images of NiMo-OS/NF (Fig. S6†) display that numerous thin nanosheets were distributed across the NF substrate without nanowire–nanosheet structures. As shown in Fig. S7,† the XRD pattern reveals only three diffraction peaks for NF(PDF#70-0908), and no obvious peaks of Ni_3S_2 and $FeMoO_4$ could be observed. This result verifies the Fe element in NFF played a vital role in the growth of Ni_3S_2–$FeMoO_4$ nanowire–nanosheet heterostructures.

The OER performance was evaluated in 1 M KOH electrolyte, based on a traditional three-electrode system. Linear scan voltammetry (LSV) curves were recorded for Ni_3S_2–$FeMoO_4$/NFF, NiMo-OS/NF, IrO_2, NiFe foam, and Ni foam (Fig. 3a). Specifically, Ni_3S_2–$FeMoO_4$/NFF electrode exhibits optimal OER activity, and offers ultralow overpotentials of only 262 mV and 331 mV to achieve 100 mA cm^{-2} and 500 mA cm^{-2}, respectively. These performance metrics are notably superior to those of NiMo-OS/NF (366 mV and 513 mV) and IrO_2/NFF (399 mV and 587 mV) to afford the same current densities. More importantly, a high current density of 1000 mA cm^{-2} can be achieved at a low overpotential of 382 mV for the Ni_3S_2–$FeMoO_4$/NFF. Notably, the overpotential of Ni_3S_2–$FeMoO_4$/NFF is obviously lower than most recently reported relevant electrocatalysts (Fig. 3b).[19–28] Furthermore, the OER activity can be optimized by varying the hydrothermal time as detailed in Fig. S8.† The results show that the Ni_3S_2–$FeMoO_4$/NFF for 10 h exhibits superior catalytic properties, which reveals that the unique nanowire–nanosheet heterostructure with larger surface area and more reactive sites could significantly improve the OER activity.

To further understand the OER kinetics, Tafel measurements were carried out. As shown in Fig. 3c, in a large current density region (near 100 mA cm^{-2}), the Ni_3S_2–$FeMoO_4$/NFF electrode offers a much lower Tafel slope of 75.77 mV dec^{-1} than those of NiMo-OS/NF (137.86 mV dec^{-1}) and IrO_2/NFF (163.6 mV dec^{-1}), demonstrating the heterointerface of $FeMoO_4$ nanosheets and Ni_3S_2 nanowires acquire the rapid OER dynamics. Additionally, electrochemical impedance spectroscopy (EIS) was measured to evaluate the charge transfer kinetics of these electrodes. As displayed in Fig. 3d, the Ni_3S_2–$FeMoO_4$/NFF electrode possesses a smaller charge transfer resistance (R_{ct}) value of 0.5 Ω than those of NiMo-OS/NF (1.5 Ω) and IrO_2/NFF (2.2 Ω). Such obviously reduced R_{ct} value shows the superior interfacial interactions were produced at the heterostructure interfaces, contributing to greatly promote the OER catalytic kinetics.[29] Moreover, the Ni_3S_2–$FeMoO_4$/NFF electrode shows a relatively lower series resistance (R_s) than other electrodes, indicating its excellent conductivity and reduced contact resistance (Fig. 3d inset). These results also reveal the nanocrystalline Ni_3S_2 nanowires with good conductivity not only support the $FeMoO_4$ nanosheets but also serve as the high-speed path for charge transfer, which further improves the charge transfer efficiency.

In addition, electrochemical surface area (ECSA) was evaluated by the double layer capacitances (C_{dl}), which was obtained from the cyclic voltammetry (CV) at different scan rates (Fig. S9†). As illustrated in Fig. 3e, the Ni_3S_2–$FeMoO_4$/NFF electrode shows a larger C_{dl} (4.64 mF cm^{-2}) than NiMo-OS/NF (2.26 mF cm^{-2}) and NFF (1.48 mF cm^{-2}), indicating that the larger ECSA can be attributed to the 3D hierarchical nanowire–nanosheet heterostructures array, which is conducive to the adsorption of water molecules and the close contact with the electrolyte.[30] Fig. S10† reveals the ECSA normalized LSV curve of Ni_3S_2–$FeMoO_4$/NFF still possess the smallest overpotential value, demonstrating the Ni_3S_2–$FeMoO_4$ heterostructure effectively enhances the intrinsic OER activity. We also measured the ECSA normalized LSV curve of Ni_3S_2–$FeMoO_4$/NFF before and after OER stability test to evaluate the intrinsic OER activity for Ni_3S_2–$FeMoO_4$/NFF. As observed in Fig. S11,† the value of C_{dl}
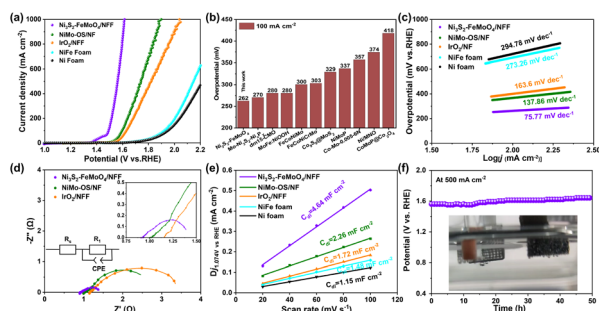
Fig. 3 OER performance. (a) LSV curves with 90% *iR* compensation of Ni foam, NiFe foam, IrO_2, NiMo-OS/NF and Ni_3S_2–$FeMoO_4$/NFF in 1 M KOH. (b) Comparison of overpotential at 100 mA cm^{-2}. (c) Tafel plots. (d) Nyquist plot and equivalent circuit, the inset image is the partial enlarged detail. (e) Double-layer capacitances. (f) Chronopotentiometry curve of Ni_3S_2–$FeMoO_4$/NFF at 500 mA cm^{-2}, and the inset is the real-time photograph of the electrode during stability test.

becomes higher due to the dissolution of Mo and more active sites in Fig. S11c.† The ECSA normalized LSV curve of Ni_3S_2–$FeMoO_4$/NFF shows that even the electrochemical active surface area increases after cycle stability test, the normalized current density trend remains consistent with that of Fig. S11d,† indicating the OER activity of Ni_3S_2–$FeMoO_4$/NFF is not affected by the electrochemical active surface area.[31] The electrochemical stability is indispensable for evaluating the OER catalytic performance. The chronopotentiometry measurements in Fig. S12† and 3f show that the Ni_3S_2–$FeMoO_4$/NFF electrode almost remains a constant potential at 100 mA cm^{-2}, and only a slight potential change even at 500 mA cm^{-2} for continuous test, demonstrating a remarkable OER stability in large current densities. In addition, it can be seen that the produced bubbles were very small and could timely detach from the Ni_3S_2–$FeMoO_4$/NFF electrode into the electrolyte in Fig. 3f (inset).[32] Thus the 3D self-supported nanowire–nanosheet architectural morphology endows the obtained electrode with abundant exposed active sites, rapid bubbles release, and timely electrolyte diffusion.

In order to further investigate the real active phase of Ni_3S_2–$FeMoO_4$/NFF, the variation of structure, composition, and valence state were analysed after OER test. The SEM of Ni_3S_2–$FeMoO_4$/NFF shows the hierarchical nanowire–nanosheet morphology is maintained well after OER test, demonstrating its excellent structural stability and corrosion resistance (Fig. S13†). As shown in Fig. S14,† the XRD spectra before and after OER test show that the characteristic peaks well index to Ni_3S_2 and no peak for $FeMoO_4$ is observed, implying the S-doped $FeMoO_4$ may reconstruct to amorphous phase after OER process. Meanwhile, the TEM image of Ni_3S_2–$FeMoO_4$ post-OER uncovers that the density of nanosheets slightly decreases (Fig. 4a). As shown in Fig. 4b, the observed interplanar spacing of 0.229 nm is well index to the (3 0 1) plane of FeOOH, indicating the $FeMoO_4$ surface was reconstructed to FeOOH after OER operation. In particular, the elemental mapping images (Fig. S15†) indicate that the Mo reduces while the Fe and O still distribute along the outer side, which agrees with the results of TEM/EDX in Table S1,† further certifying the

surface reconstruction of $FeMoO_4$. The Raman spectra of Ni_3S_2–$FeMoO_4$/NFF before and after OER process were performed in Fig. 4c. Compared to the pre-electrode, the new Raman peaks at 481 cm^{-1} and 551 cm^{-1} could be coincided with FeOOH,[33] indicating the presence of FeOOH after OER process. As observed in Fig. 4d and S16a,† the binding energies of Ni 2p and S 2p spectra have no apparent shift. Moreover, the Fe XPS spectrum shows the new peaks at 713.22 eV and 727.17 eV correspond to Fe^{3+} $2p_{3/2}$ and Fe^{3+} $2p_{1/2}$, respectively, further demonstrating that the part of Fe^{2+} are oxidized to Fe^{3+} (Fig. 4e). Besides, the Mo 3d XPS spectrum (Fig. S16b†) shows that the characteristic peak strength was weakened after OER test, indicating the loss of Mo and the formation of cationic vacancy, which can facilitate the formation of amorphous oxyhydroxide as highly active sites for OER. The O 1s spectrum shows the more concentration of oxygen vacancies (Fig. 4f), which can promote OER process.

In summary, we present a novel one-step hydrothermal strategy to fabricate hierarchical Ni_3S_2–$FeMoO_4$ nanowire–nanosheet heterostructures array in situ on the NFF substrate. Numerous ultrathin S-doped $FeMoO_4$ nanosheets are uniformly distributed on each Ni_3S_2 nanowire to form heterostructures, which offer a multitude of active sites, and leverage the multi-component interfaces to generate a synergistic effect for OER enhancement. The S-doped $FeMoO_4$ facilitates the formation of oxygen vacancy and surface reconstruction. Therefore, the self-standing and binder-free Ni_3S_2–$FeMoO_4$/NFF electrode delivers ultralow overpotentials of 262 mV and 331 mV to afford 100 and 500 mA cm^{-2}, respectively, as well as good long-term durability at large current density of 500 mA cm^{-2} for 50 h. Overall, this study demonstrates that the heterostructured Ni_3S_2–$FeMoO_4$/NFF markedly improves OER performance and open a novel approach for monolithic electrode preparation through autogenous *in situ* growth.

Conflicts of interest

There are no conflicts to declare.

Acknowledgements

References

1 H. Ding, H. F. Liu, W. S. Chu, C. Z. Wu and Y. Xie, *Chem. Rev.*, 2021, **121**, 13174–13212.

2 H. A. Sun, X. M. Xu, H. Kim, W. Jung, W. Zhou and Z. P. Shao, *Energy Environ. Mater.*, 2023, **6**, e12441.

3 H. Y. Zhong, Q. Zhang, J. C. Yu, X. Zhang, C. Wu, Y. F. Ma, H. An, H. Wang, J. Zhang, X. P. Wang and J. M. Xue, *Adv. Energy Mater.*, 2023, **13**, 2301391.

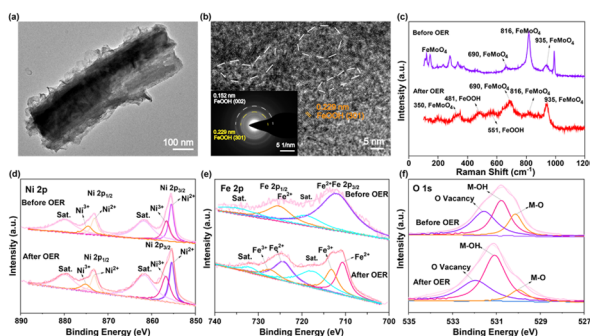**Fig. 4** Characterizations of Ni_3S_2–$FeMoO_4$ after OER operation. (a) TEM image. (b) HRTEM image, and the inset is selected area diffraction pattern. (c) Raman spectra of Ni_3S_2–$FeMoO_4$ electrode before and after OER process. (d–f) XPS spectra of Ni_3S_2–$FeMoO_4$ before and after OER process for Ni 2p, Fe 2p, and O 1s, respectively.

4 B. Chen, Z. Zhang, S. Kim, M. Baek, D. Kim and K. Yong, *Appl. Catal., B*, 2019, **259**(9), 118017.

5 J. Zhang, Y. Ye, B. Wei, F. Hu, L. T. Sui, H. W. Xiao, L. Q. Gui, J. Sun, B. B. He and L. Zhao, *Appl. Catal., B*, 2023, **330**, 122661.

6 S. Hirai, T. Ohno, R. Uemura, T. Maruyama, M. Furunaka, R. Fukunaga, W. T. Chen, H. Suzuki, T. Matsuda and S. Yagi, *J. Mater. Chem. A*, 2019, **7**, 15387–15394.

7 S. Hirai, S. Yagi, W. T. Chen, F. C. Chou, N. Okazaki, T. Ohno, H. Suzuki and T. Matsuda, *Adv. Sci.*, 2017, **4**, 1700176.

8 B. Chen, D. Kim, Z. Zhang, M. Lee and K. Yong, *Chem. Eng. J.*, 2021, **422**, 130533.

9 Y. Y. Chen, Y. Xu, S. Niu, J. Yan, Y. Y. Wu, F. K. Du, Y. Z. Zhao, Z. R. Zhu, Z. J. Jiang and X. C. Tan, *Chem. Commun.*, 2021, **57**, 4572–4575.

10 J. F. Zhang, Y. C. Hu, D. L. Liu, Y. Yu and B. Zhang, *Adv. Sci.*, 2017, **4**, 1600343.

11 L. H. Li, S. Hagiwara, C. Jiang, H. Kusaka, N. Watanabe, T. Fujita, F. Kuroda, A. Yamamoto, M. Miyakawa, T. Taniguchi, H. Hosono, M. Otani and T. Kondo, *Chem. Eng. J.*, 2023, **471**, 144489.

12 L. L. Feng, G. T. Yu, Y. Y. Wu, G. D. Li, H. Li, Y. H. Sun, T. Asefa, W. Chen and X. X. Zou, *J. Am. Chem. Soc.*, 2015, **137**, 14023–14026.

13 T. S. Song, H. Xue, J. Sun, N. K. Guo, J. W. Sun, Y. R. Hao and Q. Wang, *Chem. Commun.*, 2022, **58**, 9874–9877.

14 J. L. Zhu, J. M. Qian, X. B. Peng, B. R. Xia and D. Q. Gao, *Nano-Micro Lett.*, 2023, **15**, 30.

15 P. L. Zhai, Y. X. Zhang, Y. Z. Wu, J. F. Gao, B. Zhang, S. Y. Cao, Y. T. Zhang, Z. W. Li, L. C. Sun and J. G. Hou, *Nat. Commun.*, 2020, **11**, 5462.

16 H. X. Wang, J. S. Ren, A. J. Wang, Q. Wang, W. Zhao and L. Zhao, *Chem. Commun.*, 2022, **58**, 9202–9205.

17 F. L. Wang, X. Y. Zhang, J. C. Zhou, Z. N. Shi, B. Dong, J. Y. Xie, Y. W. Dong, J. F. Yu and Y. M. Chai, *Inorg. Chem. Front.*, 2022, **9**, 2068–2080.

18 S. Chen, Z. Xiang, Z. Xiao, K.-P. Wang, Q. Zhang and L. Wang, *Nano Res.*, 2023, **16**, 6922–6932.

19 Y. J. Mei, Y. B. Feng, C. X. Zhang, Y. Zhang, Q. L. Qi and J. Hu, *ACS Catal.*, 2022, **12**, 10808–10817.

20 Y. S. Jin, S. L. Huang, X. Yue, H. Y. Du and P. K. Shen, *ACS Catal.*, 2018, **8**, 2359–2363.

21 H. Yin, H. Xiao, R. Qin, J. Chen, F. Tan, W. Zhang, J. Zhao, L. Zeng, Y. Hu, F. Pan, P. Lei, S. Yuan, L. Qian, Y. Su and Z. Zhang, *ACS Appl. Mater. Interfaces*, 2023, **15**, 20100–20109.

22 X. Luo, P. X. Ji, P. Y. Wang, R. L. Cheng, D. Chen, C. Lin, J. A. Zhang, J. W. He, Z. H. Shi, N. Li, S. Q. Xiao and S. C. Mu, *Adv. Energy Mater.*, 2020, **10**, 1903891.

23 Y. Hao, G. Du, Y. Fan, L. Jia, D. Han, W. Zhao, Q. Su, S. Ding and B. Xu, *ACS Appl. Mater. Interfaces*, 2021, **13**, 55263–55271.

24 X. Zhang, A. Wu, D. Wang, Y. Jiao, H. Yan, C. Jin, Y. Xie and C. Tian, *Appl. Catal., B*, 2023, **328**, 122474.

25 V. Maheskumar, A. Min, C. J. Moon, R. A. Senthil and M. Y. Choi, *Small Struct.*, 2023, **4**, 2300212.

26 H. Roh, H. Jung, H. Choi, J. W. Han, T. Park, S. Kim and K. Yong, *Appl. Catal., B*, 2021, **297**, 120434.

27 L. Yi, S. Xiao, Y. Wei, D. Li, R. Wang, S. Guo and W. Hu, *Chem. Eng. J.*, 2023, **469**, 144015.

28 M. Wang, Z. Wan, X. Meng, Z. Li, X. Ding, P. Li, C. Li, J.-G. Wang and Z. Li, *Appl. Catal., B*, 2022, **309**, 121272.

29 W. H. Huang, X. M. Li, X. F. Yang, H. B. Zhang, F. Wang and J. Zhang, *Chem. Commun.*, 2021, **57**, 4847–4850.

30 Q. Liu, L. S. Xie, Z. Liu, G. Du, A. M. Asiri and X. P. Sun, *Chem. Commun.*, 2017, **53**, 12446–12449.

31 S. Hirai, S. Yagi, H. C. Oh, Y. Sato, W. Liu, E. P. Liu, W. T. Chen, A. Miura, M. Nagao, T. Ohno and T. Matsuda, *RSC Adv.*, 2022, **12**, 24427–24438.

32 N. N. Zhou, R. Liu, X. W. Wu, Y. L. Ding, X. Zhang, S. Liang, C. H. Deng, G. C. Qin, Z. L. Huang and B. Chen, *J. Power Sources*, 2023, **574**, 233163.

33 Y. Li, Y. Y. Wu, M. K. Yuan, H. R. Hao, Z. Lv, L. L. Xu and B. Wei, *Appl. Catal., B*, 2022, **318**, 121825.